FEBS Letters

FEBS PRESS science publishing by scientists

RESEARCH ARTICLE

# Unraveling membrane protein localization and interactions in nanodiscs

Young Hoon Koh, So-Jung Kim and Soung-Hun Roh

School of Biological Sciences, Institute of Molecular Biology and Genetics, Seoul National University, South Korea

**Correspondence**
S.-H. Roh, School of Biological Sciences, Institute of Molecular Biology and Genetics, Seoul National University, 1, Gwanak-ro, Gwanak-gu, Seoul, Korea
Tel: +82 10 3106 1663
E-mail: shroh@snu.ac.kr

Young Hoon Koh and So-Jung Kim contributed equally to this article

(Received 24 July 2024, revised 27 October 2024, accepted 28 October 2024)

doi:10.1002/1873-3468.15059

Edited by John Briggs

**Nanodiscs, consisting of a lipid bilayer surrounded by membrane scaffold proteins (MSPs), are extensively used to study membrane proteins (MPs) because they provide a stable lipid environment. However, the precise mechanism governing MP behavior within the nanodisc remains elusive. Here, we examined the cryo-EM structures of various MPs reconstituted in nanodiscs from EMPIAR. By analyzing the heterogeneity and interactions in the nanodiscs, we discovered that MPs display a distinct spatial preference toward the edges of the nanodisc shells. Furthermore, MPs can establish direct, amphipathic interactions with the MSPs, causing a reduction in local protein dynamics. These interactions may rearrange MSP-MSP interactions into MP-MSP interactions. Collectively, we provide structural insights into how nanodiscs contribute to MP structural behavior and dynamics.**

**Keywords:** cryo-EM; membrane proteins; membrane scaffold proteins; nanodisc

## Impact statement

Nanodiscs are used to study membrane proteins (MPs), but the mechanisms governing the behavior of MPs within nanodiscs remain elusive. Here, we provide structural insights into how nanodiscs contribute to the behavior of MPs, which will aid the interpretation of cryo-EM studies performed using nanodiscs.

Membrane proteins (MPs) are essential components in biological systems, facilitating critical functions such as signaling, transport, and enzyme activity [1]. The study of MPs has evolved remarkably over the decades, from the early biochemical assays to the sophisticated imaging techniques of today. Historically, the reconstitution of MPs poses significant challenges, primarily due to their instability and the complexity of their native environments. Early attempts at MP studies often resulted in denatured proteins, which were poorly suited for structural or functional analysis. The introduction of detergents was a major breakthrough, providing a means to extract and stabilize MPs, albeit potentially at the cost of native functionality [2].

To comprehensively address the challenges of MPs, a variety of reconstitution systems are employed with unique benefits and limitations. Among these, bicelles, lipid monolayers, SMALPs (styrene-maleic acid lipid particles), and liposomes have been instrumental [2–6]. For instance, bicelles provide a favorable environment for MPs that require a bilayer structure for functional

**Abbreviations**
CD, circular dichroism; cND, circularized nanodisc; EM, electron microscopy; EMPIAR, Electron Microscopy Public Image Archive; EPR, electron paramagnetic resonance; HDL, high-density lipoprotein; MP, membrane protein; MSP, membrane scaffold protein; ND, nanodisc; NMR, nuclear magnetic resonance; SMALP, styrene-maleic acid lipid particles.

studies, facilitating orientations that mimic natural conditions [7]. Similarly, SMALPs encapsulates MPs within native-like lipid segments, offering an alternative that preserves the protein's original lipid environment, conducive to functional and structural analyses [8].

Despite the utility of these various methods, nanodiscs have emerged as particularly popular due to their unique ability to closely mimic cell membrane environments, thereby preserving the native state of MPs [9]. Nanodiscs are discoidal protein–lipid complexes that stabilize the lipid bilayer within a scaffold made from membrane scaffold proteins (MSPs) [9]. These MSPs are typically derivatives of the human ApoA-1 protein (apolipoprotein A1), which is an amphipathic helical protein and the main component of human high-density lipoprotein (HDL) [10]. They wrap around the bilayer in an antiparallel fashion to form a belt-like structure that securely houses the hydrophobic transmembrane (TM) regions of the MPs, effectively isolating them within a stable, soluble lipid bilayer [10–12]. ApoA-1 displays considerable variability in size and composition, a characteristic also reflected in the engineered MSPs [9,13]. These MSPs are customized by modifying specific helices, either through truncation or repetition, facilitating the creation of nanodiscs in diverse sizes to suit various MPs. Such precise customization of nanodisc dimensions ensures optimal conditions for each MP, significantly improving the quality of structural analyses [9,14].

Although the structure of lipid-free ApoA-1 has long been established since 1997 [15], how MSP behaves in lipidic environment has not been clear for a long time. NMR study of the MSPΔH5 nanodisc highlighted critical features and the MSP's rearrangement to stabilize MSP-MSP and MSP-lipid interactions upon lipid incorporation [16]. Historically, phospholipid liposomes have been used to provide native, detergent-free membrane environment for MPs. However, these liposome-reconstituted MPs posed significant challenges in structural biology, as liposomes are too large for solution-state NMR and incompatible with crystallography. Phospholipid nanodisc has served as a promising method for solution-state NMR since it creates small, membrane-like particles of defined size [14,17,18]. In fact, the use of engineered shorter ApoA-1 for assembly of nanodiscs created tightly packed, small nanodisc particles that significantly improved the resolution of various MP structures using NMR [19]. Furthermore, the tailored design of these scaffold proteins not only stabilizes the MPs but also aids in elucidating their functionality in a near-native lipid environment [14,20]. The choice of lipids also plays an important role in MP and overall nanodisc stability. Variations in the lipid composition, affecting charge and length, play a crucial role in the structure and dynamics of nanodiscs by influencing their interactions with MSPs [21–23].

Besides the traditional MSP-based nanodisc technology, multiple types of nanodiscs are available. Covalently-linked MSPs form even more stable nanodiscs with precise diameters and shapes [24,25]. Reconstitution into circularized nanodiscs (cNDs) have enhanced the quality of NMR spectra for various MPs and nonenveloped viruses [24,25]. Peptide-based nanodiscs are highly dynamic, as the belt surrounding the lipid bilayer consists of multiple short peptide molecules [26,27]. These nanodiscs undergo collisions, leading to fusion and lipid exchange [26,28]. Another protein-based belt system, sphingolipid activator proteins (saposin proteins), are small, non-enzymatic proteins known for their role in modulating lysosomal activity [29]. Saposins have a unique flexible nature and a lipid-to-saposin size dependency that enables them to form nanoparticles that adjust to the size of MPs being incorporated. This is achieved by varying the number of saposin scaffold proteins used to form the belt around the MP–lipid complex [29]. Unlike MSP nanodiscs, whose size is determined by the length of the scaffold protein [9], saposins can accommodate a wide range of differently sized MPs without the need to optimize the scaffold protein to ensure that the disc is large enough to enclose the target protein [29,30].

Nanodiscs serve as an effective reconstitution method that closely replicates the native environment of MPs [9]. This, combined with the advancements in cryo-electron microscopy (cryo-EM), allows for more detailed structural analyses with enhanced resolution [31]. This benefit is emphasized in comprehensive studies of TRPV1 and NompC structures [32,33]. In these examples, nanodisc-reconstituted structures resulted in higher resolution through cryo-EM over detergent structures. Computational predictions have shown that this reduction in local dynamics arises from MP-MSP interactions, where the MP tends to localize at the edge of the nanodisc [34,35]. Experimental evidence has also suggested specific interactions between SARS-CoV-2 ORF3a and MSP within the nanodisc environment [36].

A recent study on ELIC (Erwinia ligand-gated ion channel) discovered that the protein shows different cryo-EM structures in various nanodisc environments [37]. The fluidity and elliptical deformation of nanodiscs are ongoing topics of discussion in the field. Previous literature has reported this behavior through biochemical and computational experiments, indicating

that temperature and lipid composition influence the ellipticity of MSP. Specifically, increasing the temperature results in a more circular shape [38]. Nanodiscs also become more circular when fully loaded with lipids but turn more elliptical when less than fully loaded [39–42]. However, the exact mechanisms through which nanodiscs enhance MP behaviors remain partly unclear.

In this study, we examined various MP structures reconstituted in nanodiscs from the Electron Microscopy Public Image Archive (EMPIAR) [43]. Our analysis focused on the structural heterogeneity in nanodiscs, where we observed that nanodiscs exhibit structural fluidity and elliptical deformations, consistent with previous literature. We also found that MPs move laterally within the nanodiscs. This study provides additional evidence of MP-MSP interactions, characterizing them as specific interactions between the amphipathic faces of the MSPs and the solvent–membrane interfaces of the MPs. Our research offers structural and biophysical insights into the role of nanodiscs in MP structural behavior and dynamics.

## Materials and methods

### Cryo-EM image processing for the analysis of heterogeneous nanodisc structure

Raw data of TRPV1, TRPV5 W583A, TRPV5 1–660, TRPM4, TMEM16A, TMEM16F, afTMEM16, LRRC8A, and Innexin6 were obtained from EMPIAR (Electron Microscopy Public Image Archive) (https://www.ebi.ac.uk/empiar/) for analysis. We used cryoSPARC for data processing [63]. Information on each dataset is listed in Table S1. We used MotionCor2 for motion correction of images and CTFFIND4 for CTF estimation [64]. Initial 2D templates were generated using a blob picker, and additional rounds of particle picking were carried out via template-based picking. The initial 3D model with C1 symmetry was built based on the reference 2D classes. The initial map was refined through iterative non-uniform (NU) and heterogeneous refinement processes. Once the desired resolution was reached, global and local CTF refinement followed by additional rounds of NU refinement were performed. For heterogeneity analysis of the nanodiscs, we first isolated the nanodisc density from the final map using Chimera's segment map and map eraser features [65]. We then imposed a maximum value of the Gaussian volume filter to erase the map details. A mask of the nanodisc region was created from cryoSPARC with a dilation radius and soft padding width of 3 pixels. After final processing, we performed symmetry expansion on the particles. In conjunction with the nanodisc density map, output results were used as input for 3D Variability Analysis (3DVA) [66]. A filter resolution of 7 was used to solve three modes of variability. The number of particles contributing each line in Fig. 1C are as follows: TMEM16A (176 472 particles), TMEM16F (803 940 particles), afTMEM (166 184 particles), TRPM4 (365 496 particles), TRPV1 (1 154 360 particles), TRPV5 1–660 (1 304 916 particles), TRPV5 W583A (360 908 particles), LRRC8A (1 258 710 particles), Innexin 6 (657 184 particles).

### Quantitative analysis of heterogeneity within a protein-embedded nanodisc

For quantitative analysis of heterogeneity in protein-embedded nanodiscs, each MP dataset was put into the pipeline for 3DVA (Fig. 1A). Raw data downloaded from the EMPIAR database were subjected to 2D classification, which was used for *ab initio* reconstruction. The initial 3D model was used as a model for 3D reconstruction, which was fed into the 3DVA for the symmetry expansion process. For each dataset, the MP moves relative to the MSP, which in turn also changes in shape. To quantify such complex motions, we determined that up to five different variables should be considered for a comprehensive categorization of MP particles relative to MSP within the nanodisc. As a caveat, we assumed the nanodisc adopted an elliptical shape in its 2D projection. Since the nanodisc is not an ellipsoid in 3D but rather an elliptical cylinder, we can consider only the 2D projection rather than the entire 3D structure. The comprehensible variables considered for the nanodisc include the following: the radius of the long and short axes of the ellipse, denoted as "a" and "b," respectively, and the focal point of the nanodisc "c." The sign of "c" refers to the direction of elliptical deformation, whereas the magnitude of "c" describes the degree of ellipticity of the nanodisc. We considered the variables describing the position of the MP within the nanodisc relative to the MSP as "θ" and "$\Delta R$," where "θ" is the angle formed between the long axis "a" and the line connecting the center of the nanodisc to the center of the MP, and "$\Delta R$" is the distance between the center of the nanodisc to the center of the MP.

To answer our main question of whether MP localizes to MSP more than expected, we classified three orthogonal yet complete "modes" from the 3DVA for a simpler analysis. 3DVA uses variability components to explore various motions within the dataset where it adds and subtracts corresponding density to and from the mean structure [66]. It utilizes a linear subspace model where each variability component is designed to be orthogonal to each other ($V_i^T V_j = (i = j)$) to ensure that each component or mode explains a different, independent mode of variation. In our analysis, we have also made sure that the three modes of variability satisfy "completeness," which means that the total of the particles representing all three modes represents the entire particle set of the dataset. In other words, there

are no particles unaccounted for from the sum of all particles from all three modes.

For each of the three independent modes, the motion of the MP relative to the nanodisc was such that all but one variable was fixed. For instance, two modes had varying $\Delta R$ values along a straight line with fixed $c$ value, while one mode had varying $c$ value with fixed $\Delta R$ value. We sought to analyze one of the two modes with varying $\Delta R$ and constant $c$ value to illustrate the tendency of the MPs to localize toward the edge of the nanodisc shell. Firstly,

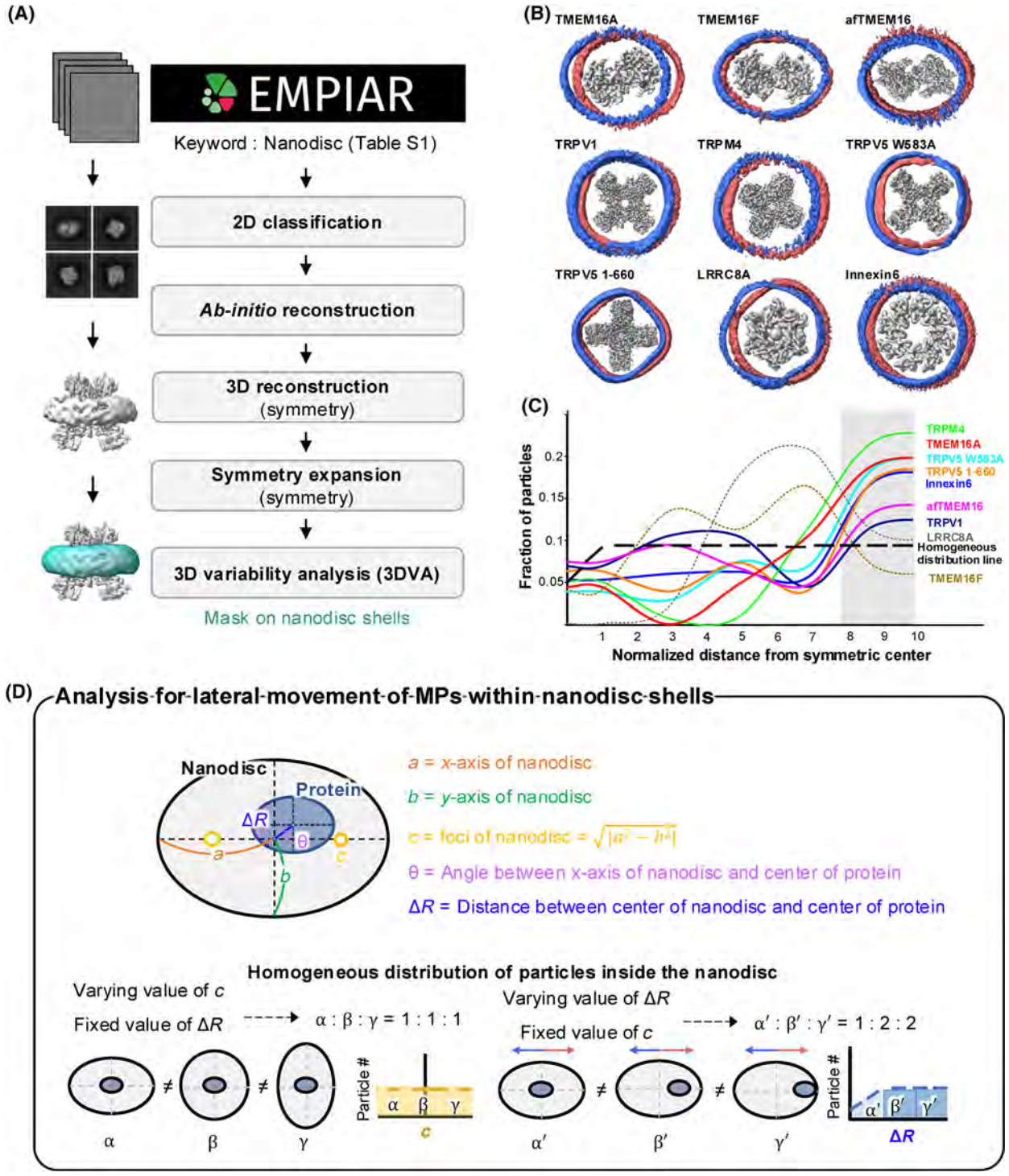

**Fig. 1.** Analysis of the heterogeneous structure of the nanodisc using quantitative model. (A) Data processing workflow using cryoSPARC for 3DVA analysis. TMEM16A is shown as a representative protein. (B) Results of 3DVA components show the direction of the subspace movement for the nine MPs used in the analysis. The relative position of the MSP to the MP in the first and last frames of the 3DVA are overlapped in blue and red. (C) The plot of the fraction of MP particles in each dataset that is at a normalized distance away from the symmetric center of the nanodisc. The black dotted line represents the fraction of particles that would exist if particles occupied the nanodisc homogeneously through each $\Delta R$ value. The color-coded plot for nine MPs shows that for some, the fractions of particles farthest away from the center (gray) are larger than expected for the homogeneous distribution of particles (ex. TRPM4, TMEM16A, TRPV5, Innexin6, afTMEM16, TRPV1). For such proteins, particles show high occupancy at the edge of the nanodisc where the MSP may stabilize the MP. (D) In the analysis of the movement of MPs within the nanodisc, we defined necessary variables ($a$, $b$, $c$, $\theta$, $\Delta R$) for our MP-embedded nanodisc model (see Materials and methods). As a control, homogeneous distributions of the particles inside the nanodisc were considered. For the case when $c$ value varies and $\Delta R$ remains constant, each value of $c$ is equally likely to occur, and thus we should obtain a horizontally flat line in the number of particles vs. $c$ value graph. When $\Delta R$ varies along a straight line while $c$ value remains constant, particles with a particular value of $\Delta R$ are degenerate. This degeneracy is twice for all values of $\Delta R$ except at $\Delta R = 0$, i.e., the center of the nanodisc. Therefore, we expect to observe a horizontally flat line in the number of particles vs $\Delta R$ value graph, except at $\Delta R = 0$ where the value is halved.

each particle in this mode is grouped into one of 20 output frames that together create the linear movement (i.e., the first frame contains particles where the MP is on one nanodisc edge while the last frame contains particles on the other edge). All other frames contain particles where MP lies sequentially in a straight line between the first and the last frame. The number of particles in each frame are determined by examining the extracted particles from micrographs in the dataset. Next, for each dataset, we determined the frame where the MP is at the center of the nanodisc. For most datasets, this was the 10th frame. We normalized the maximum value at 10 for each case and binned by five intervals (Fig. S1). The homogeneous distribution graph was calculated (Fig. 1D). For the mode where $c$ value varies and $\Delta R$ is held constant, each value of $c$ is equally probable. Therefore, the homogeneous or expected distribution is a constant line. For the modes where $\Delta R$ varies in a straight line and $c$ is constant, since each position in the linear motion is equally likely, $\Delta R$ for all values of $\Delta R > 0$ have a degeneracy of 2, which accounts for movements in either direction from the center. $\Delta R = 0$ has no degeneracy. Therefore, we obtain a homogeneous distribution of particles as shown in Fig. 1C. Therefore, the number of particles at the center of an elliptical nanodisc is half as much as the number of particles anywhere else in a homogeneous distribution (Fig. 1D).

Quantifying the overall motion of the MP inside the nanodisc that is constantly changing its shape, as is the case with a full dataset of particles, is complicated. This would require the consideration of all five variables ($a$, $b$, $c$, $\theta$, $\Delta R$) in the calculation process (Fig. 1D) and is beyond the scope of this paper for answering our main question of whether MP localizes more near the MSP than expected.

## Structure visualization

We displayed published structural maps of various MPs using the Coulombic surface coloring feature in Chimera [65] to highlight the surface charges. We applied a 3 Å low-pass filter to the nanodisc density and the MP in cryoSPARC [63]. In Chimera, we separated the density of the MSP from the filtered map through a segmentation process.

## Identification of the sequence fragment in MSP1D1

We isolated only the EM density corresponding to the MSP from a 3 Å low-pass filtered map of the cytochrome bd-I oxidase protein using the same process described above. The map was re-segmented to observe the side chain density map of the MSP. The candidate sequence came from the full sequences of MSP1D1 used in the nanodisc reconstitution of cytochrome bd-I oxidase (Fig. S3A). The high-resolution MSP map was composed of an eight-turn α-helix. Based on 3.6 amino acids per turn of α-helix, we estimated the total length as 29 amino acids. To determine the candidate sequences within the MSP, we used the 3$^{rd}$, 10$^{th}$, and 18$^{th}$ bulky amino acids from the MP contact side as a reference within the high-resolution MSP map (Fig. S3B). For the fitting, the 3$^{rd}$ residue in the chain was designated F, K, Y, or R as the bulkiest side chains, which left 30 candidate MSP sequences that might fit into the MSP map. The 10$^{th}$ and 18$^{th}$ residues also showed bulky side chain densities, allowing the elimination of residues A, P, G, and V occupying those sites. Through this process of elimination, we had seven final candidate sequences (Fig. S3C). Initial model fitting for all seven candidate MSP sequences was done using ISOLDE, an MD simulation-based software [67]. We used the default setting values for all parameters except for α-helix restrain. We improved the accuracy of the model fitting using real-space refinement software from Phenix [67,68]. We calculated the $Q$-score from the fitted models of density resolvability for protein and quantitative evaluation [45]. In the 3.0 Å filtered map, the $Q$-score value for each candidate sequence was compared to the average $Q$-score value to determine the best candidate.

### V-ATPase $V_0$ image analysis

The V-ATPase $V_0$ image analysis was carried out with cryoSPARC [63], with the first 3D reconstruction of the V-ATPase $V_0$ complex performed in RELION 3.0 [45,69,70] with a 2.81 Å resolution. The 3D classification included 476 k processed particles, the map from cryoSPARC, and the mask of the nanodisc region of the $V_0$ complex depicted using Chimera [65]. A regularization parameter T of 4 was used with no image alignment. The resulting classes were categorized by whether the MSP strands were visible. The high-resolution MSP group had 203 419 particles (42.75% of total particles), whereas the low-resolution MSP group had 272 394 particles (57.25%). Using the NU refinement program from cryoSPARC, three sets of 3D reconstructions were performed with the total number of particles, the high-resolution MSP group, and the low-resolution MSP group. The input volume was the same as the map used in RELION. The resulting output volume and the mask of only the MP region were used as input for the local refinement process in RELION to improve local resolution in the MP region. The total particles, high-resolution, and low-resolution groups had final resolutions of 2.86, 2.92, and 2.99 Å, respectively.

### Quantitative analysis for structural dynamics

In cryoSPARC [63], we calculated the local resolution of the MSP using the output volume and mask derived from local refinement. In Chimera [65], MSP surface coloring was performed from the output volume of the local refinement process. The local resolution output volume was used as the input volume data value. The color key was set in five intervals (2.5, 2.9, 3.3, 3.6, and 3.9 Å). In Phenix, we performed real-space refinement with default settings using the V-ATPase $V_0$ complex map and model (6M0R) as the input. From this refinement, we obtained the atomic displacement parameter value (B-factor) for each residue in the protein.

### Transmembrane length estimation using CHIMERAX

We used CHIMERAX [49] to estimate the transmembrane length of all of the membrane proteins (MPs) considered in this study. PDB files of all reprocessed MPs were examined on CHIMERAX to identify polar/non-polar and charged/non-charged regions. Precise non-polar and non-charged edges were estimated for distance measurement using the distance feature on CHIMERAX. We report the TM lengths in Table S1 and the summarized result in Fig. S5.

### Data sharing plans

Further information and requests for resources and reagents should be directed to and will be fulfilled by the Lead Contact, Soung-Hun Roh (shroh@snu.ac.kr).

## Results

### Membrane proteins have a spatial preference toward the edge of the nanodisc shells

López et al. conducted molecular dynamics simulations by modeling the activated, membrane-embedded BAX conformation within a nanodisc system to explore its behavior in the lipid bilayer environment. In their analysis, López et al. [34] showed in part of their analysis that BAX moved toward the edge of the nanodisc to make various contact with the MSP, where it was stabilized. Once BAX initially attached to the MSP, there was no detachment during the simulation timescales. Other studies showed this movement is entropy-driven [35]. To further investigate the general spatial preference of MPs within the nanodisc shells, we revisited nine datasets of various MPs reconstituted in nanodiscs from EMPIAR (Table S1). These datasets were chosen to encompass a wide set of MSP and lipids used for nanodisc reconstitution (Table S1). We characterized the heterogeneity of the nanodisc shells using a two-step approach (Fig. 1A). First, we generated consensus maps by aligning the MPs to establish a common reference frame using single particle analysis. Second, we classified the heterogeneity exhibited by the MSP relative to the MPs by focus-classifying on the nanodisc shells. We describe the detailed processing methods in the sections 'Cryo-EM image processing for the analysis of heterogeneous nanodisc structure' and 'Quantitative analysis of heterogeneity within a protein-embedded nanodisc'. We observed an improvement in the intensity of the partial belt-like densities surrounding the MPs, which could potentially be attributed to the MSP. The analysis for all MPs displayed notable changes in the shape of the nanodiscs. Specifically, the nanodisc shells adopted an elliptical shape with varying degrees of ellipticity (Fig. 1B). These findings collectively suggest that the MPs within the nanodiscs are freely able to move and explore areas within the nanodisc relative to the MSP (Fig. S1B). Likewise, the MSP is able to bend and adopt an elliptical conformation. These observations were reflected in the MP spatial distribution and the MSP shape in the 3D Variability Analysis (3DVA) results.

To delineate the relative location of the MPs within the nanodiscs, we focused on discerning a subset of states that manifested linear motion of the MPs from one end of the MSP to the other (varying $\Delta R$) while maintaining the overall nanodisc shape (constant $c$ value) (Fig. 1B, Fig. S1A). We scrutinized the particle population distribution using a quantitative model

(Fig. 1B–D). The details for how the lines were computed are described in the Materials and methods section. For reference, we included a control scenario where we posited homogeneous distribution of particles throughout the linear motion from one end of the nanodisc to the other. Our analysis revealed a pronounced enrichment of MPs at the periphery of the nanodisc shells (Fig. 1C) compared to the control distribution. Indeed, seven out of nine distinct MP datasets analyzed exhibited this characteristic. Although the consensus view in the field suggests that the MPs are predominantly localized in the central region of the nanodisc surrounded by the lipid molecules by floating in a sea of lipids, this depiction may inaccurately imply that the protein is passively floating in the lipid environment. On the contrary, our collective observations revealed a more dynamic behavior, supporting previous observations of an entropic-driven migration of MP toward the nanodisc edge [34,35]. Given that each dataset contains hundreds of thousands of nanodisc particles, our observation that most datasets show this tendency of MP to preferentially position toward the rim provides reasonable evidence. From this result, we sought to see whether there are potential interactions between the nanodisc shell (MSP) and the MP itself that accounts for unusual localization of the protein at the edge of the nanodisc.

## Characterization of MP-MSP interactions

A significant portion of the acquired maps demonstrated ambiguous characteristics within the nanodisc shells, which can be ascribed to the inherent flexibility and dynamics of the MSP with the protein under investigation (Fig. 2A). By applying a low-pass filter on the cryo-EM map of cytochrome bd-I oxidase (EMD-4908) without further reprocessing, we observed distinct belt-like density features predominantly located close to the membrane–solvent interface on the transmembrane helices of MPs (Fig. 2A). Based on the resolution of the cytochrome structure, we opted to utilize a 3 Å low-pass filter to effectively eliminate high-frequency noise density while retaining genuine, low-frequency density. By applying this filter uniformly across the entire map, we ensure the preservation of both high- and low-resolution features pertaining to both the MSP and the MP. The presence of distinct belt-like density close to the membrane–solvent interface suggests that there are interactions between the MSP and MPs where the MSP may create local energy minima through their direct interactions. To characterize the interactions between the MPs and MSP, we analyzed the nanodisc-reconstituted maps from the EM database (Fig. S2). Despite the limited resolution in the nanodisc shells that prevented the elucidation of the MSP-MP interactions in most cases, a notable exception was observed for the cytochrome bd-I oxidase protein map (EMD-4908) [44]. This map exhibited a high-resolution density, corresponding to a partial density of the alpha helix from the single-strand MSP in direct contact with the cytochrome bd-I oxidase (Fig. 2A). The fragment of the MSP map revealed a distinct density pattern consisting of eight α-helical turns, corresponding to 29 amino acids. Bulky side chain densities were observed at specific positions ($n + 3$, $n + 10$, and $n + 18$, where $n$ is the residue at the N terminus) within the 29-residue segment (Fig. S3B). By excluding small residues (e.g., alanine, glycine, serine, or proline) at these positions, seven candidate sequences among MSP1D1 were selected and subsequently refined into the density (Fig. 2B(i), Fig. S3C). To find the best matching candidate, we employed $Q$-score analysis, which provides a quantitative assessment of the resolvability score for each atom and backbone [45]. Our analysis revealed that the sequence 37–65 exhibited a significantly higher residue score compared to the other candidates (Fig. 2B(ii)). This sequence had an optimal fit within the segmented MSP density (Fig. 2B(iii)). Therefore, the observed fragment density corresponded to a specific region of MSP1D1, and this defined feature implied the presence of a constrained interaction between MSP1D1 and cytochrome bd-I oxidase.

The MSP1D1 fragment was positioned perpendicularly to the luminal side of the membrane–solvent interface, and the helical pitches of the MSP matched with the groove of the transmembrane helices of cytochrome bd-I oxidase. An examination of the interface revealed the presence of a combination of polar and hydrophobic residues (Fig. 3A), resulting in a pronounced degree of polar and hydrophobic complementarity within the specific region. Notably, the MSP exhibited negatively charged residues, specifically E46, E53, D57, and E61, which emerged as potential candidates for interactions with the positively charged residues K123 and K361 within the cytochrome bd-I oxidase (Fig. 3C(i)). We also observed that the hydrophobic side of the MSP was oriented toward the hydrophobic transmembrane region of the MP (Fig. 3C(ii)). As depicted in a helical wheel representation (Fig. 3B), the interactions between MSP and MPs are characterized by highly favorable binding between the amphipathic faces of the MSP and the solvent–membrane interface of the MPs. In other words, the polar/charged MSP residues from the contact helix interact with the MP near the solvent side while the hydrophobic MSP residues interact with the

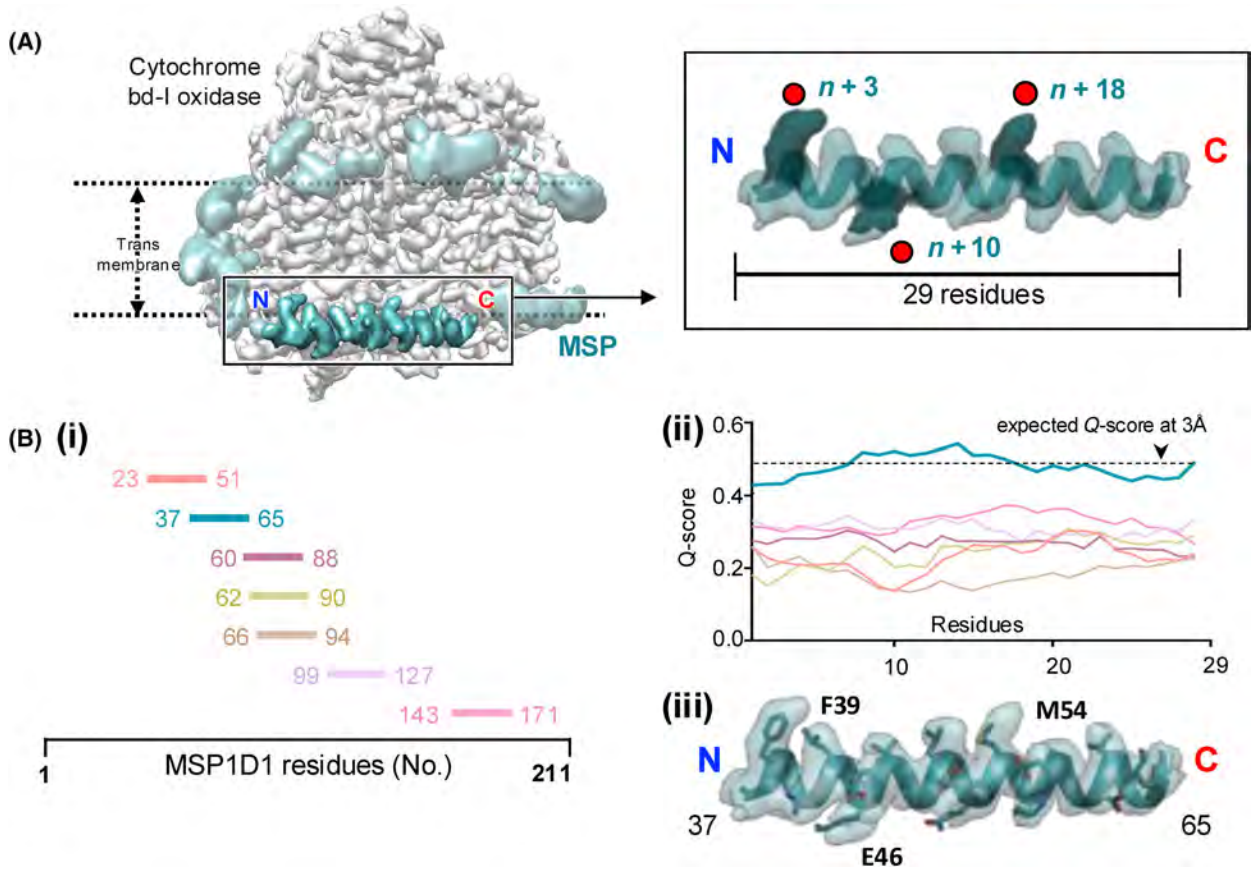


**Fig. 2.** Resolving the structure of MSP involved in MP-MSP interactions. (A) (*left*) Processed cryo-EM density map of cytochrome bd-I oxidase (gray) and MSP (cyan). The partial high-resolution MSP map on the edge of the transmembrane region of the MP is highlighted in the rectangular box. (*right*) A close-up of the high-resolution MSP region. Based on the number of helical turns, 29 residues are estimated to fit into the density. The bulky side chain densities of the $n + 3$, $n + 10$, and $n + 18$ positions are highlighted. (B) (i) The seven 29-residue candidate sequences within MSP1D1 for best fit into the high-resolution MSP density map are color-coded. (ii) The *Q*-score for each candidate sequence is shown. The MSP sequence 37–65 (cyan) displayed the highest *Q*-score and was designated the best candidate for the high-resolution MSP density. (iii) The MSP sequence 37–65 (QEFWDNLEKETEGLRQEMSKDLEEVKAKV) best fits into the high-resolution MSP density.

transmembrane region of the MP. While this interaction could exhibit specificity as is the case in cytochrome bd-I oxidase, it may also display dynamic features with weak and heterogeneous constraints in most MPs (Fig. S2).

## MP-MSP interactions contribute to high-resolution structure

We wanted to test the influence of the close interactions of MSPs on the behavior and structures of the MPs. For this purpose, we selected the vacuolar-type ATPase (V-ATPase) $V_0$ complex from *S. cerevisiae* because its structure has been resolved under different solubilizing conditions, including detergent ($V_0$Det, 3.2 Å), amphipol ($V_0$Amp, 3.9 Å), and nanodisc ($V_0$ND, 2.7 Å) [46–48] (Table S2). By comparing the features among the different maps, we observed a significant improvement in global resolution in the $V_0$ND reconstruction compared to the other conditions (Fig. 4A). Notably, while $V_0$ND exhibited a uniform signal intensity throughout the entire map, the maps for $V_0$Det and $V_0$Amp displayed more varied signal intensities and higher B-factors, particularly on subunits c(3)-c(8) and d (Fig. 5A). Considering a similar number of particles were used for the final reconstruction, this enhanced global and local resolution in the $V_0$ND reconstruction suggested that the particles reconstituted in the nanodiscs might possess reduced structural variability.

To clarify the relationship between the presence of the nanodisc and localized MP structure, we

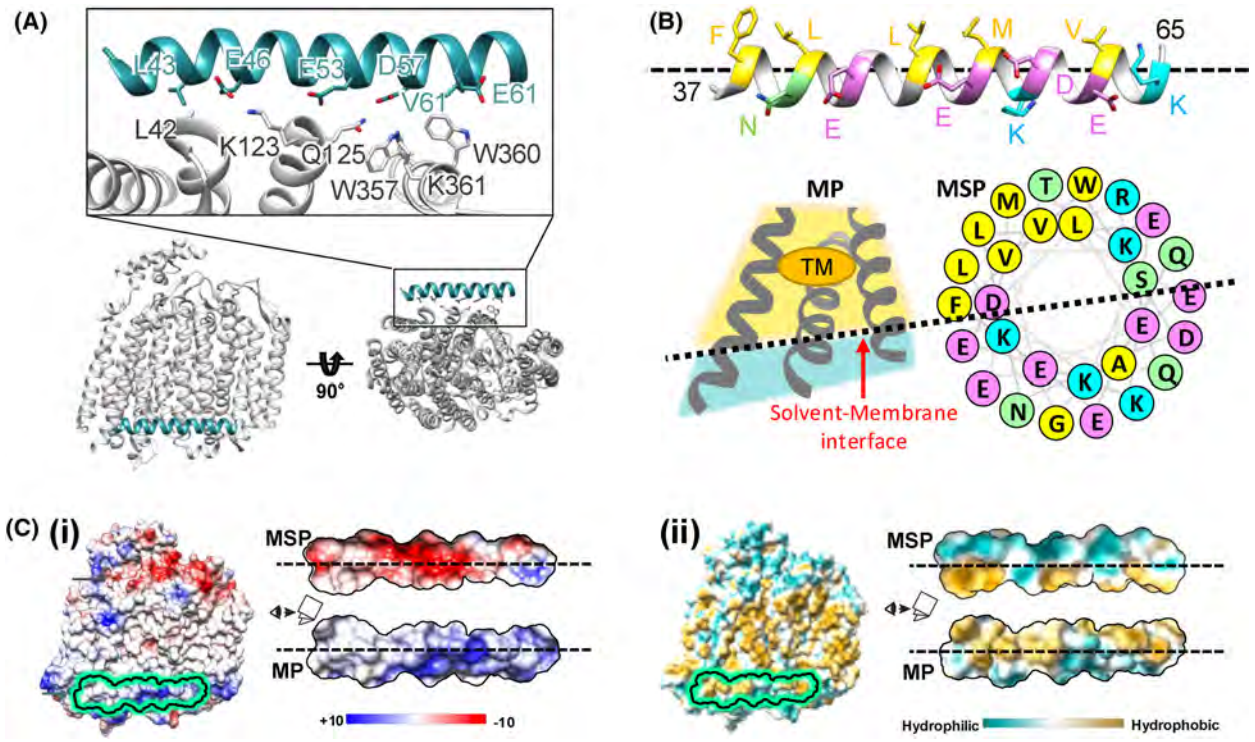


**Fig. 3.** Characterization of specific MP-MSP interactions. (A) Site of interaction between cytochrome bd-I oxidase (gray) and the high-resolution MSP (cyan) models. Relevant residues in the interaction are highlighted in both the MSP and MP. (B) The helical wheel representation of sequence 37–65 shows the side of the MSP interacting with the cytochrome bd-I oxidase. Residues are color-coded based on their hydrophobicity, hydrophilicity, and charge. The MSP interacts with the MP at the solvent–membrane interface at the edge of the transmembrane region such that polar/charged residues interact with the solvent side while the hydrophobic residues interact with the hydrophobic transmembrane region. (C) (i) (*left*) Electrostatic potential map of MP with the site of contact with the high-resolution MSP map highlighted. (*right*) The negatively charged residues on the contact face of the MSP can interact with the positively charged residues on the cytochrome bd-I oxidase. (ii) (*left*) Hydrophobic surface of the MP with the site of contact with the high-resolution MSP map highlighted. (*right*) A combination of the hydrophobic and hydrophilic regions in both MSP and the MP strengthens their interaction.

performed a comprehensive analysis of the $V_0$ND particle images. By reconstructing the consensus map and applying a focused classification on the nanodisc shells, we separated the $V_0$ particles and subsequently grouped them based on the density of the MSP features. Group A (43% of the total particles) exhibited distinct and well-defined belt-like MSP densities, whereas group B (57% of the particles) displayed partial and weak MSP density (Fig. 4B(i)). The detailed classification method is described in Fig. S4. The difference map between these groups clearly demonstrated the disparity in the upper two MSP densities, confirming the effectiveness of particle classification in detecting the presence of MSPs. Within group A, we observed that the top and bottom MSPs were positioned closely within 10 Å of the $V_0$'s c-ring, leaving limited space for lipid molecules. This observation suggested the potential for a direct interaction between the c-ring and the MSPs.

The 3D reconstruction of both groups exhibited distinct and well-defined MP features, with similar overall average resolutions of approximately 2.9 Å for group A and 3.0 Å for group B (Fig. 4B(ii)). However, a closer analysis of the local areas between the two groups revealed a significantly higher resolution and a lower average B-factor in group A, specifically in the cytosolic side of the c-ring region. Interestingly, this region aligned with the cytosolic region of the c-ring, where a noticeable discrepancy in resolution was observed between $V_0$ND and $V_0$Det (Fig. 4A). This consistent finding suggested that defined MSP interactions play a role in stabilizing the MP.

We also analyzed the per-residue B-factor changes (ΔB-factor values) between groups A and B to assess the degree of stabilization resulting from the MSP interactions. For each residue, the ΔB-factor value was calculated by subtracting the B-factor value of group B from that of group A. We focused on eight identical

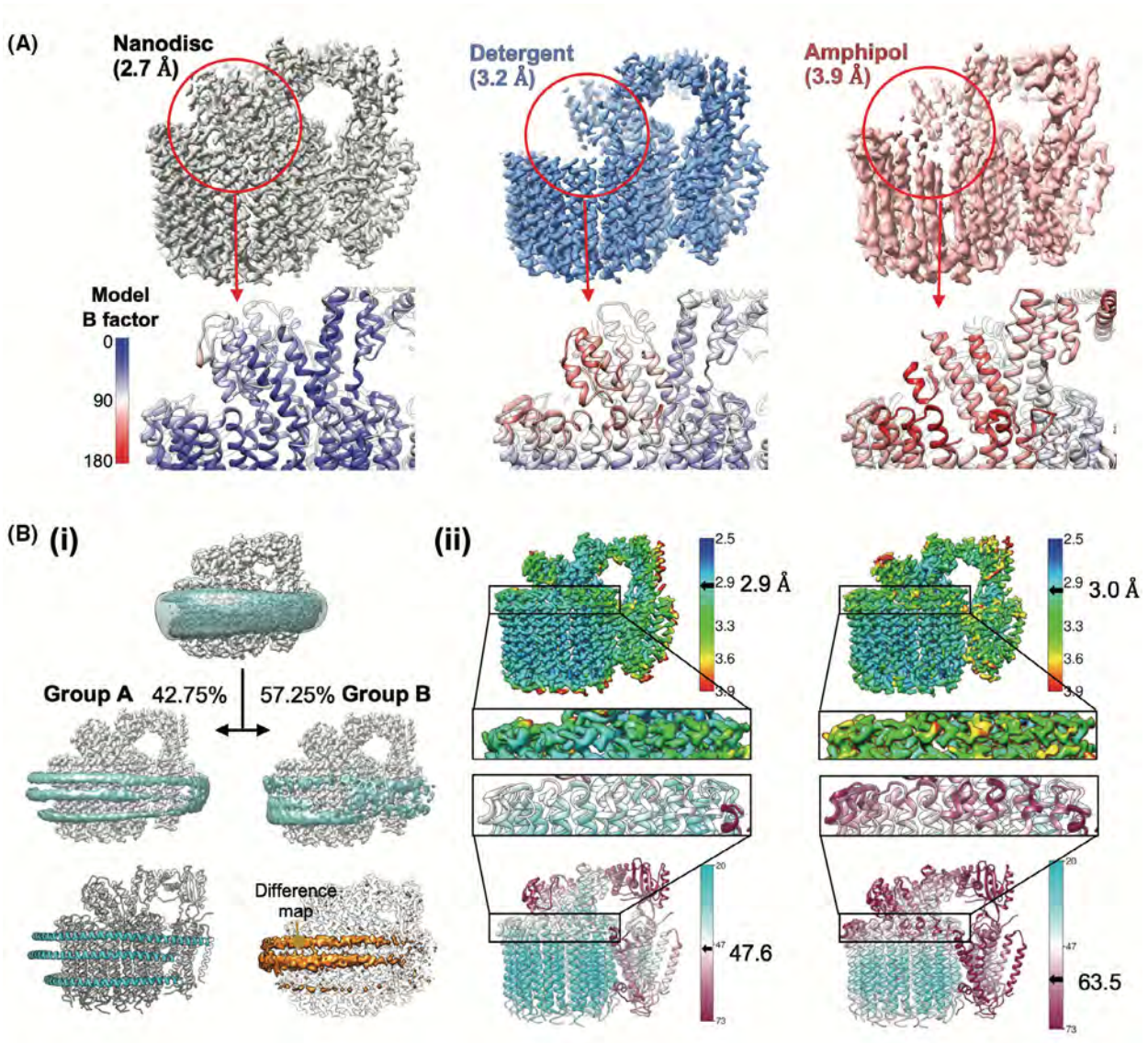


**Fig. 4.** Nanodisc contributes to high-resolution structure. (A) Resolution and B-factor value comparisons among known cryo-EM structures of V-ATPase $V_0$ complex in the nanodisc (*left*), detergent (*middle*), and amphipol (*right*). Specific regions in the structure with notable local resolution and B-factor differences are highlighted. (B) (i) Processed EM density map of the $V_0$ complex in the nanodisc (*top*) was classified into two groups of particles for focused refinement. Group A (42.75% of total particles) contains particles with well-defined MSP features, while group B (57.25% of total particles) contains those with obscure or poorly defined MSP features (*middle*). The three distinct MSP strands in the nanodisc surrounding the $V_0$ complex are shown as a model (*bottom left*). The difference in the EM map between groups A and B (*bottom right*) isolates the MSP density responsible for improving the local resolution and B-factor in group A relative to group B. (ii) Resolution and B-factor value comparisons between group A (*left*) and B (*right*). The upper c-ring region with large deviations in local resolution and B-factor is highlighted.

c-subunits (c(1) through c(8)) that exhibited varying exposure within the nanodisc shells (Fig. 5A). Notably, subunit c(1) interacted with another subunit a, whereas c(2) was partially exposed to the phospholipid and had limited contact with the MSP. In contrast, c(3) through c(8) were exposed to the MSPs. When comparing chains c(1) and c(2), where the MP does not directly interact with the MSPs, the alterations in the B-factors had no significant distinctions (Fig. 5B). Conversely, subunits c(3) through c(8) displayed notable negative ΔB-factor values on average. Subunits c(6), c(7), and c(8) exhibited especially large deviations

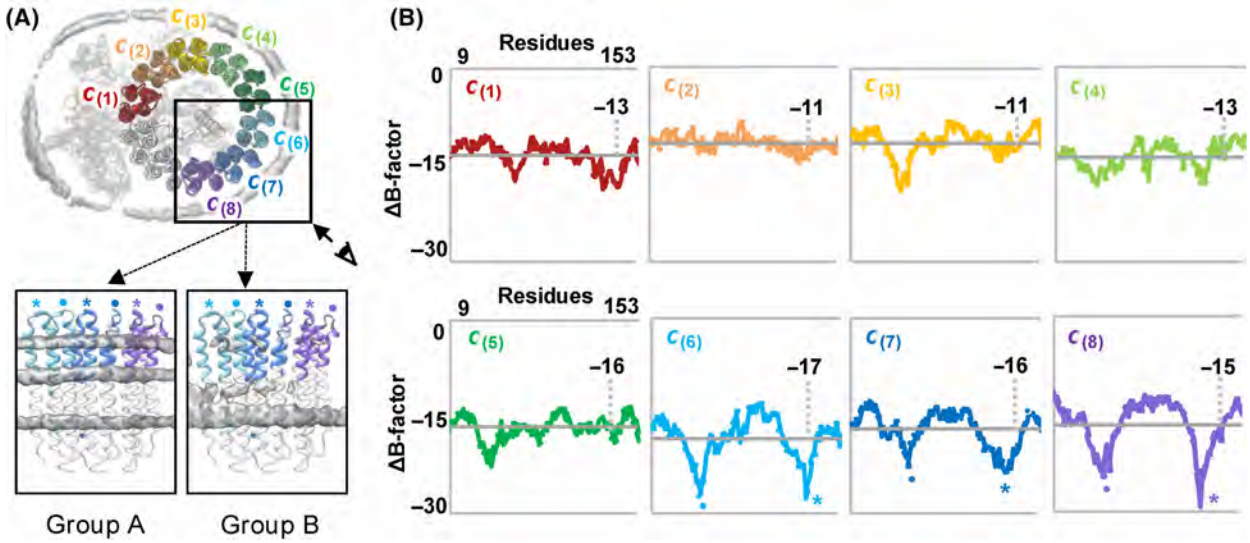


**Fig. 5.** B-factor analysis of V-ATPase reveals reduced local dynamics in protein in contact with MSP. (A) Top view of the $V_0$ complex in the nanodisc with c-ring subunits color-coded. In the c(6), c(7), and c(8) subunits, the MSP density differences between groups A and B were the most conspicuous. (B) Plot of ΔB-factor values for each residue in the c-ring subunits is shown. ΔB-factor values were calculated by subtracting the B-factor values of group B from those of group A. The largest deviations were observed in the c(6), c(7), and c(8) subunits; the residues with the most noticeable differences are highlighted with dots and stars.

in their B-factor values (Fig. 5B). Taking a closer look at the structure, we also observed the largest difference in MSP features between groups A and B in the c(6), c(7), and c(8) subunits. In group A, we observed that all MSP strands surrounding the residues in these subunits displayed distinct MSP features, whereas in group B, we observed a distinct MSP feature only in the bottom strand (Fig. 5A). Correspondingly, the residues in the c(6), c(7), and c(8) subunits with the largest ΔB-factor values were in the cytosolic region that interacted with the top strand of the MSP (Fig. 5B, dot and star). Taken together, these data demonstrated that the reduced local dynamics of the MSP surrounding the MP conferred stable direct interactions with the MP itself in those regions to lower their B-factor values and reduce protein dynamics. These findings suggest that direct interaction with the MSP could enhance the resolution of MP.

## Multivalent MSPs are involved in the formation of nanodiscs

Since MSP is derived from apolipoprotein A1, which consists of two aligned strands, it has been commonly assumed that MSPs in nanodiscs adopt a configuration with two strands. Through detailed classification focusing on MSPs within the nanodisc, we identified three MSP belts within the V-ATPase $V_0$ complex (Fig. 6A). Through masked classification where we focused on densities resembling individual belt, we discovered that, based on regrouping via feature clarity, 25% of the particles displayed two distinct belts on the top and bottom while 75% showed three belts, including a middle one (Fig. 6B). The existence of the third MSP strand suggests that a conventional MSP dimer may be insufficient to fully stabilize the hydrophobic surface of the V-ATPase. The top and bottom MSPs were positioned near the interfaces between the membrane and solvent in $V_0$. The middle MSP strand was located at a greater distance from the $V_0$ but at an approximate distance of 13 Å from the top MSP, corresponding to the typical spacing between helices in apolipoproteins (Fig. 6A). Analysis of the database also showed three MSP strands in glucosyltransferase Alg6 (PDB 6SNI, EMD-10258) and arabinofuranosyltransferase D (AftD) (PDB 6W98, EMD-21580) (Fig. S2). We then sought whether there is a correlation between the transmembrane (TM) length of the MP and the number of MSP strands in the nanodisc surrounding each protein. We estimated the TM length for all reconstructed protein structures considered in our study using to measure the distances [49] (see Materials and methods). These lengths are reported in Table S1 and are summarized in Fig. S5. The nine MPs exhibiting two MSP strands in their nanodisc displayed a TM length range of 30.2–39.4 Å (Table S1, Fig. S5). The three MPs exhibiting three MSP strand densities had the following TM lengths: V-ATPase $V_0$

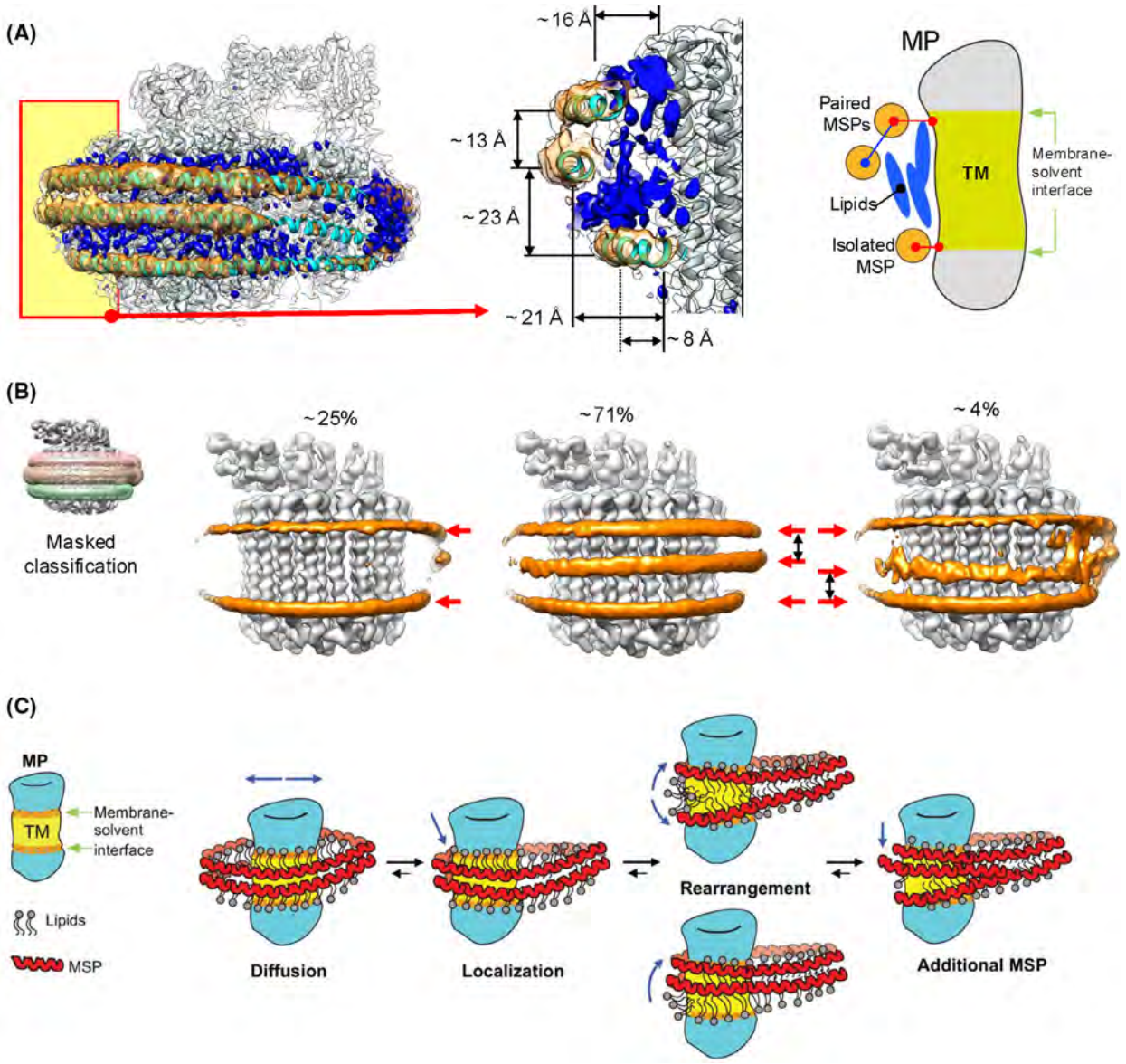


**Fig. 6.** Multivalent MSP binding to membrane proteins and stabilizing mechanism. (A) (*left*) V-ATPase $V_0$ complex model (gray) and density map (white), including the MSP model (cyan) and map (orange). The density maps corresponding to the lipid molecules are colored in blue. The site of the MP-MSP interactions is highlighted with a yellow box for a zoomed-in view (*middle*). The distances between the top, middle, and bottom MSP strands and membrane protein were approximately 16, 21, and 8 Å, respectively. The distance between the top and middle MSP strands was about 13 Å, while that between the middle and bottom strands was approximately 23 Å. The lipid molecules could occupy the space between the top and middle MSP strands and the $V_0$ complex but not the space between the bottom MSP strand and the $V_0$ (*right*). A schematic view of the MP-MSP interactions. The top and bottom MSP strands surround the MP at the membrane–solvent interface. The bottom strand forms a direct and stable interaction with the MP through a lipid-free local environment (red line). The top strand interacts with both the middle strand of the MSP (blue line) and the MP (red line). (B) Masked classification was performed, focusing on densities resembling individual belts. Based on feature clarity, 25% of the particles displayed two distinct belts on the top and bottom, while approximately 75% exhibited three belts, including a middle one. MSP is highlighted in orange, with the red arrowhead indicating its location. (C) The schematic illustration depicts the nanodisc stabilization process after initial assembly. The MSP bilayer (red) envelops the MP (cyan) and phospholipid (PL) (gray), supported by salt-bridge interactions between the MSP strands. The MP undergoes diffusive movement within the nanodisc, and the MP and MSP can make contact. The MSP-MSP salt-bridge interaction is then converted to MP-MSP interactions. The overall nanodisc adopts an elliptical shape during this process. If the MP has a TM length above a certain threshold, the two strands of the MSP come far enough apart to allow the presence of a third MSP strand, further stabilizing the MP through MP-MSP contacts.

complex (45.2 Å), Alg6 (42.6 Å), AftD (48.3 Å) (Table S1, Fig. S5). From this, we observed a strong correlation between the TM length and the number of MSP strands in the nanodisc (Fig. S5). The longer the transmembrane length, the further the two original MSP strands in the nanodisc are likely to come apart when they contact the MP. As a result, the third strand is more likely to occupy the larger space created between the two MSP strands.

Given that the transmembrane domains of MPs typically exceed a length of 30 Å, typical stacking of MSP strands composed of MSP-MSP interactions is not long enough to cover the entire transmembrane domain. Alternatively, our findings indicated a reorganization of the interactions from MSP-MSP into MP-MSP. Consequently, the presence of an additional MSP might serve to shield the lipid environment surrounding the MPs (Fig. 6C). While it is unclear how the third strand is recruited, this observation implied that the MSPs engaged in a dynamic interplay involving both traditional and complementary interactions with neighboring MSPs and direct interactions with MPs. Such a combination of interactions could preserve nanodisc morphology while simultaneously accommodating lipids and solubilizing the MPs.

## Discussion

The use of nanodiscs for the reconstitution of MPs has gained considerable popularity as a method for biophysical and biochemical studies of MPs in their native environment. In our experimental analysis, we observed that MPs exhibited significant spatial preference toward the edges of the nanodisc shells, allowing them to establish contact with the MSPs. These interactions are dynamic, occurring between the amphipathic surfaces of the MSPs and the interface between the solvent and the membrane of the MPs. The amphipathic MP-MSP interactions were also observed by Kern et al. in their cryo-EM structure of the nanodisc-reconstituted SARS-CoV-2 ORF3a protein, where they resolved partial MSP1E3D1 density at the membrane–solvent interface of the MP [36]. This interface involves both polar and non-polar residues from MSP, which interact with corresponding polar and non-polar residues from ORF3a. Along with the MP-MSP interaction characterized in the structure of cytochrome bd-I oxidase, this provides further support for the amphipathic interaction of MSP at the membrane–solvent interface. This spatial preference for the nanodisc periphery can perhaps be attributed to the relatively thinner lipid bilayer in this region compared to the center of the nanodisc [50]. The spatial preference of the MPs within the nanodisc may also influence the overall shape of the nanodisc. In our heterogeneity analysis, we noted that nanodiscs across various datasets exhibited deformed or elliptical shapes. Previous studies suggest that this behavior may be due to the lack of lipid packing in local areas near the MSP [39–42]. The establishment of MP-MSP interactions potentially lowers the local concentration of lipids in the area of contact.

The resolution of cryo-EM structures of MP is influenced by multiple factors, from the nature of the particular membrane protein to the degree of coverage by the membrane mimetic. Furthermore, there are both reasons for and against the resolution of the cryo-EM maps of MP in nanodisc being higher than those in detergent [32,33,51–54]. Therefore, it is difficult to generalize whether the resolution of cryo-EM map in nanodisc would be higher or lower than in detergent. Recent literature has shown, however, that nanodisc-reconstituted MP cryo-EM structures could yield higher resolution over their detergent-embedded counterparts [33]. Our study provides support to this notion by highlighting the role of nanodisc in enhancing MPs' resolution due to reduced variability in the protein conformation (Figs 4B(ii) and 5B). Although nanodiscs are generally regarded as providing a native-like lipid environment for proteins [9], the interactions between MPs and MSP are not physiological and may influence the proteins conformation, deviating from its natural environment. In fact, Dalal et al. observed that the use of varying MSP sizes influenced the structures of the reconstituted protein [37]. The smaller MSP tends to bind the protein more tightly, potentially altering the properties of the lipid bilayer or directly interacting with the protein of interest, while larger MSP tends to provide a more dynamic lipid environment [37]. While the impact of these MP-MSP interactions on the activity of purified proteins remains uncertain, it is necessary for the scientific community to carefully choose the appropriate type of nanodisc to optimize structural experiments and minimize the risk of introducing non-physiological conditions.

Emerging techniques such as saposin nanodiscs have been successfully used to stabilize and purify a wide range of MPs, including GPCRs [55], peptide transporters [30], ion channels [56], and solute carriers [57]. Saposin nanodiscs have been shown to produce higher resolution structures compared to traditional nanodiscs, as they bind more tightly around the transmembrane regions of MPs without incorporating as large a portion of lipids [30]. This interaction between saposin and MPs may be similar to the MP-MSP interaction we observed in our study, although the number of

saposins appears to be guided by the size of the MP, indicating more protein-specific interactions. Thus, saposin nanodiscs may offer a convenient alternative to traditional nanodiscs for structural biology. However, higher resolution by reduced dynamics does not necessarily imply that the structure is in a native-like conformation. We may require a more thorough comparison and analysis to study the impact that the reconstitution environment provides to the MP.

Since the cryo-EM structures from this study involve samples in cryogenic temperatures, the resulting rigidity in the lipids may favor the specific binding of an MP to the MSP. The cooling rate from sample vitrification ($10^5$–$10^6$ $K{\cdot}s^{-1}$) is fast and therefore preserves many features in a lipid bilayer such as lateral organization of lipids. Nonetheless, it is not fast enough to prevent ordering of lipid chains through gauche-to-trans isomerization that drives the bilayer into a gel phase for a phase transition [58]. While there is little experimental evidence to identify the exact role of temperature on the lipid state, some MD simulation results exist. López et al. [34] showed through coarse-grain and all-atom MD simulations on empty nanodiscs that at temperature below the gel-to-liquid melting transition temperature ($T_m$), two lipid phases were present: an inner region resembling a gel phase and an outer region resembling a liquid crystalline phase. At temperature above $T_m$, lipids distributed uniformly as liquid crystalline state, displaying more fluidity. When they added the MP to the nanodisc, in both temperature conditions, the MP moved toward the edge of the nanodisc [34]. While López et al. did not study cryogenic temperatures in the simulations, they showed that the rigidity of lipids does not appear to be the main reason for MP-MSP interaction.

From our analyses, we propose the characteristics of MPs reconstituted in nanodiscs (Fig. 6C). During the initial reconstitution of MPs into nanodiscs, the hydrophobic regions of the MPs are reconstituted by the phospholipid bilayer, which is stabilized by the surrounding MSP proteins. The MSP strands are initially stacked to each other and stabilized by a complementary charge interaction [59]. MPs in the nanodisc undergo lateral diffusion and are entropically stabilized at the nanodisc edge [35]. MPs establish contacts with the proximal MSPs, converting MSP-MSP strand interactions into MP-MSP interactions. During this reorganization, each MSP shifts to the membrane–solvent interface of the MPs. Due to the amphipathic nature of MSPs, both hydrophobic and charge–charge interactions form between the MPs and MSPs, generating a stabilized MP-embedded nanodisc. As the two strands of MSP are rearranged to the membrane–solvent interfaces on the MPs, the hydrophobic TM region of the MPs can be exposed to an aqueous solution, which may destabilize the protein. To accommodate this effect, an additional MSP strand surrounds the exposed hydrophobic region for stabilization. This behavior of nanodiscs to form three strands has already been reported in the V-ATPase structure [48].

Our measurement of the transmembrane lengths of MPs revealed that there is a correlation between the physical length of the TM region of the MP and the number of MSP strands the nanodisc adopts (Table S1, Fig. S5). As the MP moves toward the edge of the nanodisc, it increases the contact with the MSP strands. The strength of the contact between the MSP and the MP pulls the two MSP strands apart. For MPs with longer TM lengths, the space created between the separated MSP strands is large enough to adopt a third strand. This extra strand may provide thermodynamic stability to the MP as it interacts with the MSP and prevents the hydrophobic region of the MP from being exposed to the hydrophilic environment. As for how the third strand is introduced into the nanodisc, it likely happened during the nanodisc reconstitution process. When detergent-purified MPs are mixed with MSP and lipids, the detergent molecules surrounding the MPs must be replaced. This replacement typically occurs over a period ranging from 2 h to overnight, allowing the system sufficient time to reach an equilibrium state. In this dynamic environment, where detergent, lipid, and MSP coexist, additional MSP strands may become integrated into existing nanodisc structures.

The length of the transmembrane region of the MP may be correlated with whether two or three MSP strands wrap around the MP in nanodisc assembly, especially if MP-MSP contacts are allowed to occur. Nanodisc assembly conditions—including the choice of lipids, MSPs, MPs, and their ratios [9–11]—have a significant impact on the final nanodisc structure [9–11]. Since lipid binding to MPs is a prerequisite for MSP stabilization, it is logical that the presence of three-belt MSPs could be mitigated by adjusting the system to achieve better hydrophobic matching, particularly by optimizing the hydrophobic thickness of the membrane based on the acyl chain length of the lipids used. We acknowledge that the choice of MSP is a critical consideration for protein size; however, the transmembrane height of the protein has not yet been extensively factored into these decisions. Most experiments typically use similar lipids, including Soy PC, POPC, POPE, E. coli total lipids, or yeast polar lipids (Table S1), where the dominant acyl chains are C16–C18 in length [60]. Prokaryotic lipids, in contrast,

often have shorter acyl chains (C12–C18) compared to eukaryotic lipids (C16–C22) [61,62]. Based on our comparison, we did not identify a clear relationship between lipid composition and MP behavior in nanodiscs. The effect of different lipid environments on MP-MSP interactions, driven by variations in lipid acyl chain lengths, should be systematically explored through well-designed biochemical studies and structural analyses in the future.

In our analysis, we utilized ten nanodisc datasets of various MPs with different MSPs and lipids (Table S1). Each dataset contains hundreds of thousands of particles from which we average signals that exhibit MP and MSP behaviors that we observed. Ten datasets, therefore we believe, are sufficient to draw conclusions that MP can localize to the edge of the nanodisc to make specific, stabilizing interactions with the MSP. While we were unable to identify any MSP, lipid or even MP dependencies with these behaviors, we have achieved our goal of highlighting that such MP-MSP interactions occur experimentally and can influence the local dynamics of the MP. Ultimately, this contact impacts the resolution of the final cryo-EM structure.

## Acknowledgements

This work was supported by the National Research Foundation of Korea (2020R1A5A1018081, 2021M3A9I4021220, 2020R1A6C101A183, RS-2024-00344154 and RS-2024-00440289) and the SUHF fellowship to S-HR. We thank members of Center for Macromolecular and Cell Imaging (CMCI) for their discussions and suggestions.

## Author contributions

Conceptualization: S-HR; Investigation: YHK, S-JK; Writing: YHK, S-JK, and S-HR; Funding Acquisition: S-HR.

## Peer review

The peer review history for this article is available at https://www.webofscience.com/api/gateway/wos/peer-review/10.1002/1873-3468.15059.

## Data accessibility

All processed data were derived from raw data obtained from EMPIAR, EMDB, and/or PDB. TRPV1 – EMPIAR (10059), EMDB (8117), PDB (5IRX). TRPV5 (1–660) – EMPIAR (10255), EMDB (0593), PDB (6O1N). TRPV5(W583A) – EMPIAR (10253), EMDB (0605), PDB (6O1U). TRPM4 – EMPIAR (10127), EMDB (7133), PDB (6BQV). TMEM16A – EMPIAR (10123), EMDB (7095), PDB (6BGI). TMEM16F – EMPIAR (10280), EMDB (20246), PDB (6P48). afTMEM16 – EMPIAR (10240), EMDB (8959), PDB (6E1O). LRRC8A – EMPIAR (10258), EMDB (0562), PDB (6NZW). Innexin 6 – EMPIAR (10291), EMDB (9973), PDB (6KFH). Cytochrome bd-I oxidase – EMPIAR (−), EMDB (4908), PDB (6RKO). V-ATPase $V_0$ complex – EMPIAR (−), EMDB (30035), PDB (6M0R). Alg6 – EMPIAR (−), EMDB (10258), PDB (6SNI). AftD – EMPIAR (10399), EMDB (21580), PDB (6W98).

## References

1 Sligar SG and Denisov IG (2021) Nanodiscs: a toolkit for membrane protein science. *Protein Sci* **30**, 297–315.
2 Seddon AM, Curnow P and Booth PJ (2004) Membrane proteins, lipids and detergents: not just a soap opera. *Biochim Biophys Acta* **1666**, 105–117.
3 Postis V, Rawson S, Mitchell JK, Lee SC, Parslow RA, Dafforn TR, Baldwin SA and Muench SP (2015) The use of SMALPs as a novel membrane protein scaffold for structure study by negative stain electron microscopy. *Biochim Biophys Acta* **1848**, 496–501.
4 Bayburt TH and Sligar SG (2003) Self-assembly of single integral membrane proteins into soluble nanoscale phospholipid bilayers. *Protein Sci* **12**, 2476–2481.
5 Dufourc EJ (2021) Bicelles and nanodiscs for biophysical chemistry. *Biochim Biophys Acta Biomembr* **1863**, 183478.
6 Brockman H (1999) Lipid monolayers: why use half a membrane to characterize protein-membrane interactions? *Curr Opin Struct Biol* **9**, 438–443.
7 Shen H-H, Lithgow T and Martin L (2013) Reconstitution of membrane proteins into model membranes: seeking better ways to retain protein activities. *Int J Mol Sci* **14**, 1589–1607.
8 Kamilar E, Bariwal J, Zheng W, Ma H and Liang H (2023) SMALPs are not simply nanodiscs: the polymer-to-lipid ratios of fractionated SMALPs underline their heterogeneous nature. *Biomacromolecules* **24**, 1819–1838.
9 Denisov IG and Sligar SG (2017) Nanodiscs in membrane biochemistry and biophysics. *Chem Rev* **117**, 4669–4713.
10 Davidson WS and Hilliard GM (2003) The spatial organization of apolipoprotein A-I on the edge of discoidal high density lipoprotein particles: a mass specrometry study. *J Biol Chem* **278**, 27199–27207.
11 Patel H, Ding B, Ernst K, Shen L, Yuan W, Tang J, Drake LR *et al.* (2019) Characterization of

apolipoprotein A-I peptide phospholipid interaction and its effect on HDL Nanodisc assembly. *Int J Nanomedicine* **14**, 3069–3086.
12 Li Y, Kijac AZ, Sligar SG and Rienstra CM (2006) Structural analysis of nanoscale self-assembled discoidal lipid bilayers by solid-state NMR spectroscopy. *Biophys J* **91**, 3819–3828.
13 Kontush A and John Chapman M (2011) High-Density Lipoproteins: Structure, Metabolism, Function and Therapeutics. John Wiley & Sons, Hoboken, NJ.
14 Ritchie TK, Grinkova YV, Bayburt TH, Denisov IG, Zolnerciks JK, Atkins WM and Sligar SG (2009) Chapter 11 – reconstitution of membrane proteins in phospholipid bilayer nanodiscs. *Methods Enzymol* **464**, 211–231.
15 Borhani DW, Rogers DP, Engler JA and Brouillette CG (1997) Crystal structure of truncated human apolipoprotein A-I suggests a lipid-bound conformation. *Proc Natl Acad Sci USA* **94**, 12291–12296.
16 Bibow S, Polyhach Y, Eichmann C, Chi CN, Kowal J, Albiez S, McLeod RA, Stahlberg H, Jeschke G, Güntert P *et al.* (2017) Solution structure of discoidal high-density lipoprotein particles with a shortened apolipoprotein A-I. *Nat Struct Mol Biol* **24**, 187–193.
17 Judge PJ and Watts A (2011) Recent contributions from solid-state NMR to the understanding of membrane protein structure and function. *Curr Opin Chem Biol* **15**, 690–695.
18 Hagn F, Nasr ML and Wagner G (2018) Assembly of phospholipid nanodiscs of controlled size for structural studies of membrane proteins by NMR. *Nat Protoc* **13**, 79–98.
19 Hagn F, Etzkorn M, Raschle T and Wagner G (2013) Optimized phospholipid bilayer nanodiscs facilitate high-resolution structure determination of membrane proteins. *J Am Chem Soc* **135**, 1919–1925.
20 Johansen NT, Tidemand FG, Nguyen TTTN, Rand KD, Pedersen MC and Arleth L (2019) Circularized and solubility-enhanced MSPs facilitate simple and high-yield production of stable Nanodiscs for studies of membrane proteins in solution. *FEBS J* **286**, 1734–1751.
21 Sweeney DT, Krueger S, Sen K and Hackett JC (2022) Structures and dynamics of anionic lipoprotein Nanodiscs. *J Phys Chem B* **126**, 2850–2862.
22 Surewicz WK, Epand RM, Pownall HJ and Hui SW (1986) Human apolipoprotein A-I forms thermally stable complexes with anionic but not with zwitterionic phospholipids. *J Biol Chem* **261**, 16191–16197.
23 Epand RM, Segrest JP and Anantharamaiah GM (1990) Thermodynamics of the binding of human apolipoprotein A-I to dimyristoylphosphatidylglycerol. *J Biol Chem* **265**, 20829–20832.
24 Nasr ML, Baptista D, Strauss M, Sun Z-YJ, Grigoriu S, Huser S, Plückthun A, Hagn F, Walz T, Hogle JM *et al.* (2017) Covalently circularized nanodiscs for studying membrane proteins and viral entry. *Nat Methods* **14**, 49–52.
25 Miehling J, Goricanec D and Hagn F (2018) A split-intein-based method for the efficient production of circularized nanodiscs for structural studies of membrane proteins. *Chembiochem* **19**, 1927–1933.
26 Carlson ML, Young JW, Zhao Z, Fabre L, Jun D, Li J, Li J, Dhupar HS, Wason I, Mills AT *et al.* (2018) The peptidisc, a simple method for stabilizing membrane proteins in detergent-free solution. *elife* **7**, e34085.
27 Orwick MC, Judge PJ, Procek J, Lindholm L, Graziadei A, Engel A, Gröbner G and Watts A (2012) Detergent-free formation and physicochemical characterization of nanosized lipid-polymer complexes: Lipodisq. *Angew Chem Int Ed Engl* **51**, 4653–4657.
28 Ravula T, Ishikuro D, Kodera N, Ando T, Anantharamaiah GM and Ramamoorthy A (2018) Real-time monitoring of lipid exchange via fusion of peptide based lipid-nanodiscs. *Chem Mater* **30**, 3204–3207.
29 Flayhan A, Mertens HDT, Ural-Blimke Y, Martinez Molledo M, Svergun DI and Löw C (2018) Saposin lipid nanoparticles: a highly versatile and modular tool for membrane protein research. *Structure* **26**, 345–355.e5.
30 Frauenfeld J, Löving R, Armache JP, Sonnen AF, Guettou F, Moberg P, Zhu L, Jegerschöld C, Flayhan A, Briggs JA *et al.* (2016) A saposin-lipoprotein nanoparticle system for membrane proteins. *Nat Methods* **13**, 345–351.
31 Januliene D and Moeller A (2021) Single-particle Cryo-EM of membrane proteins. *Methods Mol Biol* **2302**, 153–178.
32 Gao Y, Cao E, Julius D and Cheng Y (2016) TRPV1 structures in nanodiscs reveal mechanisms of ligand and lipid action. *Nature* **534**, 347–351.
33 Autzen HE, Julius D and Cheng Y (2019) Membrane mimetic systems in CryoEM: keeping membrane proteins in their native environment. *Curr Opin Struct Biol* **58**, 259–268.
34 López CA, Swift MF, Xiao-Ping X, Hanein D, Volkmann N and Gnanakaran S (2019) Biophysical characterization of a Nanodisc with and without BAX: an integrative study using molecular dynamics simulations and Cryo-EM. *Structure* **27**, 988–999.e4.
35 Orioli S, Henning CG, Hansen and Arleth L (2021) Ab initio determination of the shape of membrane proteins in a nanodisc. *Acta Crystallogr D Struct Biol* **77**(Pt 2), 176–193.
36 Kern DM, Sorum B, Mali SS, Hoel CM, Sridharan S, Remis JP, Toso DB, Kotecha A, Bautista DM and

Brohawn SG (2021) Cryo-EM structure of SARS-CoV-2 ORF3a in lipid nanodiscs. *Nat Struct Mol Biol* **28**, 573–582.
37 Dalal V, Arcario MJ, Petroff 2nd JT, Tan BK, Dietzen NM, Rau MJ, Fitzpatrick JAJ, Brannigan G and Cheng WWL (2024) Lipid nanodisc scaffold and size alter the structure of a pentameric ligand-gated ion channel. *Nat Commun* **15**, 25.
38 Skar-Gislinge N, Simonsen JB, Mortensen K, Robert F'l, Sligar SG, Møller BL, Bjørnholm T and Arleth L (2010) Elliptical structure of phospholipid bilayer nanodiscs encapsulated by scaffold proteins: casting the roles of the lipids and the protein. *J Am Chem Soc* **132**, 13713–13722.
39 Shih AY, Denisov IG, Phillips JC, Sligar SG and Schulten K (2005) Molecular dynamics simulations of discoidal bilayers assembled from truncated human lipoproteins. *Biophys J* **88**, 548–556.
40 Denisov IG, Grinkova YV, Lazarides AA and Sligar SG (2004) Directed self-assembly of monodisperse phospholipid bilayer nanodiscs with controlled size. *J Am Chem Soc* **126**, 3477–3487.
41 Denisov IG, McLean MA, Shaw AW, Grinkova YV and Sligar SG (2005) Thermotropic phase transition in soluble nanoscale lipid bilayers. *J Phys Chem B* **109**, 15580–15588.
42 Whorton MR, Bokoch MP, Rasmussen SGF, Huang B, Zare RN, Kobilka B and Sunahara RK (2007) A monomeric G protein-coupled receptor isolated in a high-density lipoprotein particle efficiently activates its G protein. *Proc Natl Acad Sci USA* **104**, 7682–7687.
43 Iudin A, Korir PK, Salavert-Torres J, Kleywegt GJ and Patwardhan A (2016) EMPIAR: a public archive for raw electron microscopy image data. *Nat Methods* **13**, 387–388.
44 Safarian S, Hahn A, Mills DJ, Radloff M, Eisinger ML, Nikolaev A, Meier-Credo J, Melin F, Miyoshi H, Gennis RB *et al.* (2019) Active site rearrangement and structural divergence in prokaryotic respiratory oxidases. *Science* **366**, 100–104.
45 Pintilie G, Zhang K, Zhaoming S, Li S, Schmid MF and Chiu W (2020) Measurement of atom resolvability in Cryo-EM maps with Q-scores. *Nat Methods* **17**, 328–334.
46 Vasanthakumar T, Bueler SA, Di W, Beilsten-Edmands V, Robinson CV and Rubinstein JL (2019) Structural comparison of the vacuolar and Golgi V-ATPases from saccharomyces cerevisiae. *Proc Natl Acad Sci USA* **116**, 7272–7277.
47 Mazhab-Jafari MT, Rohou A, Schmidt C, Bueler SA, Benlekbir S, Robinson CV and Rubinstein JL (2016) Atomic model for the membrane-embedded VO Motor of a Eukaryotic V-ATPase. *Nature* **539**, 118–122.
48 Roh S-H, Shekhar M, Pintilie G, Chipot C, Wilkens S, Singharoy A and Chiu W (2020) Cryo-EM and MD infer water-mediated proton transport and autoinhibition mechanisms of Vo complex. *Sci Adv* **6**, eabb9605.
49 Meng EC, Goddard TD, Pettersen EF, Couch GS, Pearson ZJ, Morris JH and Ferrin TE (2023) UCSF ChimeraX: tools for structure building and analysis. *Protein Sci* **32**, e4792.
50 Maingi V and Rothemund PWK (2021) Properties of DNA- and protein-scaffolded lipid Nanodiscs. *ACS Nano* **15**, 751–764.
51 Dang S, Feng S, Tien J, Peters CJ, Bulkley D, Lolicato M, Zhao J, Zuberbühler K, Ye W, Qi L *et al.* (2017) Cryo-EM structures of the TMEM16A calcium-activated chloride channel. *Nature* **552**, 426–429.
52 Frauenfeld J, Gumbart J, Sluis EO, Funes S, Gartmann M, Beatrix B and Mielke T (2011) Cryo-EM structure of the ribosome–SecYE complex in the membrane environment. *Nat Struct Mol Biol* **18**, 614–621.
53 Wu M and Lander GC (2020) How low can we go? Structure determination of small biological complexes using single-particle cryo-EM. *Curr Opin Struct Biol* **64**, 9–16.
54 Schmidt-Krey I and Rubinstein JL (2011) Electron cryomicroscopy of membrane proteins: specimen preparation for two-dimensional crystals and single particles. *Micron* **42**, 107–116.
55 Lavington S and Watts A (2020) Lipid nanoparticle technologies for the study of G protein-coupled receptors in lipid environments. *Biophys Rev* **12**, 1287–1302.
56 Kintzer AF, Green EM, Dominik PK, Bridges M, Armache JP, Deneka D, Kim SS, Hubbell W, Kossiakoff AA, Cheng Y *et al.* (2018) Structural basis for activation of voltage sensor domains in an ion channel TPC1. *Proc Natl Acad Sci USA* **115**, E9095–E9104.
57 Nguyen NX, Armache JP, Lee C, Yang Y, Zeng W, Mootha VK, Cheng Y, Bai XC and Jiang Y (2018) Cryo-EM structure of a fungal mitochondrial calcium uniporter. *Nature* **559**, 570–574.
58 Sharma KD, Heberle FA and Waxham MN (2023) Visualizing lipid membrane structure with cryo-EM: past, present, and future. *Emerg Top Life Sci* **7**, 55–65.
59 Klon AE, Segrest JP and Harvey SC (2002) Molecular dynamics simulations on discoidal HDL particles suggest a mechanism for rotation in the apo A-I belt model. *J Mol Biol* **324**, 703–721.
60 Mörs K, Roos C, Scholz F, Wachtveitl J, Dötsch V, Bernhard F and Glaubitz C (2013) Modified lipid and protein dynamics in nanodiscs. *Biochim Biophys Acta* **1828**, 1222–1229.
61 Krishnan A, McNeil BA and Stuart DT (2020) Biosynthesis of fatty alcohols in engineered microbial cell factories: advances and limitations. *Front Bioeng Biotechnol* **8**, 610936.

62 Li-Beisson Y, Shorrosh B, Beisson F, Andersson MX, Arondel V, Bates PD, Baud S, Bird D, Debono A, Durrett TP *et al.* (2013) Acyl-lipid metabolism. *Arabidopsis Book* **11**, e0161.
63 Punjani A, Rubinstein JL, Fleet DJ and Brubaker MA (2017) cryoSPARC: algorithms for rapid unsupervised Cryo-EM structure determination. *Nat Methods* **14**, 290–296.
64 Rohou A and Grigorieff N (2015) CTFFIND4: fast and accurate defocus estimation from electron micrographs. *J Struct Biol* **192**, 216–221.
65 Pettersen EF, Goddard TD, Huang CC, Couch GS, Greenblatt DM, Meng EC and Ferrin TE (2004) UCSF Chimera–a visualization system for exploratory research and analysis. *J Comput Chem* **25**, 1605–1612.
66 Punjani A and Fleet DJ (2021) 3D variability analysis: resolving continuous flexibility and discrete heterogeneity from single particle Cryo-EM. *J Struct Biol* **213**, 107702.
67 Croll TI (2018) ISOLDE: a physically realistic environment for model building into low-resolution electron-density maps. *Acta Crystallogr D Struct Biol* **74**(Pt 6), 519–530.
68 Adams PD, Afonine PV, Bunkóczi G, Chen VB, Davis IW, Echols N, Headd JJ, Hung L-W, Kapral GJ, Grosse-Kunstleve RW *et al.* (2010) PHENIX: a comprehensive python-based system for macromolecular structure solution. *Acta Crystallogr D Biol Crystallogr* **66**(Pt 2), 213–221.
69 Zivanov J, Nakane T, Forsberg BO, Kimanius D, Hagen WJ, Lindahl E and Scheres SH (2018) New tools for automated high-resolution Cryo-EM structure determination in RELION-3. *elife* **7**, e42166.
70 Scheres SH (2012) RELION: implementation of a Bayesian approach to cryo-EM structure determination. *J Struct Biol* **180**, 519–530.

## Supporting information

Additional supporting information may be found online in the Supporting Information section at the end of the article.

**Fig. S1.** 3DVA results used on quantitative model to analyze the distribution of membrane protein within the nanodisc.

**Fig. S2.** Nanodisc shells at low-threshold display.

**Fig. S3.** The amino acid sequence of MSP1D1 and candidates used for model fitting.

**Fig. S4.** Classification and refinement of V-ATPase V0 complex particles by clarity of the MSP density yields differences in local resolution and B-factor values.

**Fig. S5.** Length of the transmembrane region in membrane proteins correlates with ability to adopt three MSP strands in nanodisc.

**Table S1.** Datasets utilized from EMPIAR/EMDB/PDB Database.

**Table S2.** Datasets of membrane proteins with structures solubilized in detergent and/or amphipol.